Supplementary data

Supplementary Information

Photo-rechargeable zinc ion capacitors using $MoS_2/NaTaO_3$/CF dual-acting electrodes prepared by photodeposition method

Aliakbar Mozafari [a], Mohamad Mohsen Momeni [a*], Ali Naderi [b], Byeong-Kyu Lee [b*]

[a] *Department of Chemistry, Isfahan University of Technology, Isfahan 84156-83111, Iran*

[b] *Department of Civil and Environment Engineering, University of Ulsan, Daehakro 93, Namgu, Ulsan, 680-749, Republic of Korea*

[*]Corresponding author. Email address: mm.momeni@cc.iut.ac.ir

[*]Corresponding author. Email address: bklee@ulsan.ac.kr

Supplementary data

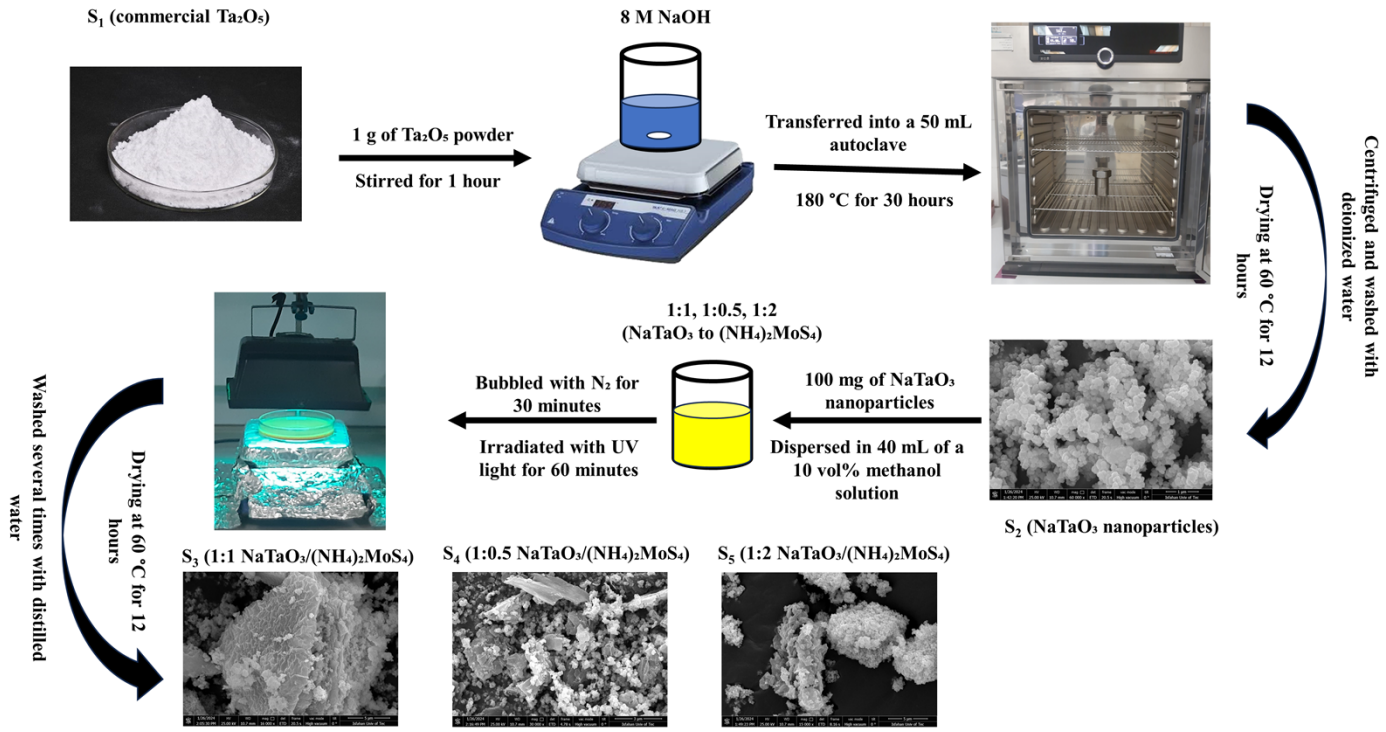

Fig. S1 Schematic of preparation of $MoS_2/NaTaO_3$ heterostructure.

Supplementary data

Fig. S2(a) displays the XRD patterns of the pristine carbon felt (CF) and the activated carbon felt (ACF). The carbon felt (CF) substrate exhibits a broad peak around 2θ=26°, which is characteristic of the graphitic carbon structure. In contrast, the activated carbon felt (ACF) shows a significantly sharper and more intense peak at the same position, indicating an increase in the graphitization degree and the crystallinity of the carbon material upon activation. The XRD analysis presented in Fig. S2(b) compares the CF substrate with the $NaTaO_3$ phase. The distinct peaks observed in the $NaTaO_3$ spectrum confirm the successful synthesis of the sodium tantalate compound. The XRD analysis of the $MoS_2/NaTaO_3$/CF heterostructure, as shown in Fig. S2(c), reveals an intriguing structural phenomenon. As previously observed, no distinct peaks corresponding to the MoS_2 phase were identified in the diffraction pattern. This observation suggests a high degree of dispersion and intimate integration of the MoS_2 component within the heterostructure, without the formation of large, segregated MoS_2 crystallites. Interestingly, a pronounced peak shift is observed when comparing the $MoS_2/NaTaO_3$/CF heterostructure (Fig. S2(c)) with the standalone $NaTaO_3$ pattern (Fig. S2(b)). The peaks in the heterostructure are shifted towards lower 2θ values, indicating an expansion of the $NaTaO_3$ lattice parameters. This shift in the diffraction signals points to the potential formation of a new phase or the intercalation of the MoS_2 component within the $NaTaO_3$ crystal structure. Such structural modifications at the MoS_2-$NaTaO_3$ interface suggest the occurrence of strong interfacial interactions and the emergence of novel structural arrangements within the heterostructured system. The integration of the MoS_2 phase into the $NaTaO_3$ lattice may lead to the stabilization of unique crystal phases or the

Supplementary data

introduction of lattice strain, both of which could significantly influence the functional properties of the final heterostructure.

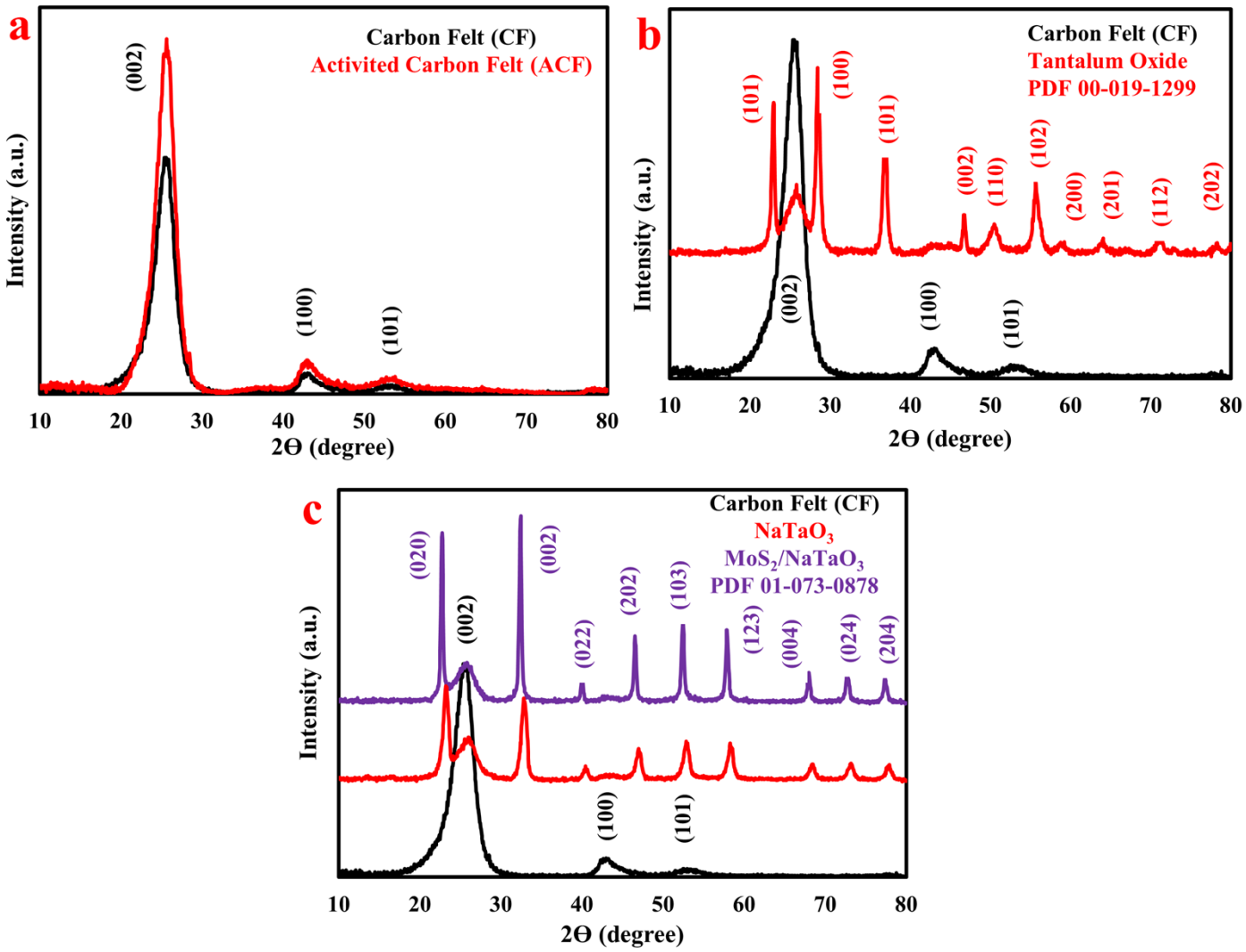

Fig. S2 (a) XRD patterns of CF and ACF (b), XRD patterns of CF and Ta_2O_5 and (c) XRD patterns of CF, $NaTaO_3$ and $MoS_2/NaTaO_3$.

Supplementary data

Figs. S3(a-d) provided appear to be microscopic views of a carbon felt, before and after some kind of treatment or modification. Figs. S3(a,b) shows the untreated or unmodified carbon felt structure. The image reveals a network of carbon felt with a smooth, uniform appearance. Figs. S3(c,d), on the other hand, shows the carbon felt after surface activation or cleaning treatment, using UV light. This treatment has visibly altered the surface of the carbon felt, making them appear rougher and more textured compared to the untreated material in the first image. The changes in surface morphology observed between the images suggest that the treatment, likely a UV light exposure, has modified the surface characteristics of the carbon felt. This kind of surface activation is often done to improve the material's properties, such as enhanced adsorption capacity, catalytic activity, or wettability, depending on the intended application of the carbon felt. Figs. S3(e-h) shows the heterostructures images of $NaTaO_3$/CF and MoS_2/$NaTaO_3$/CF, respectively. The elemental analysis provide further information about the composition of these heterostructured materials. EDX analysis of $NaTaO_3$/CF (Fig. S3(i)) shows the presence of sodium (Na), tantalum (Ta), and carbon (C), confirming the formation of the $NaTaO_3$/CF heterostructure. EDX analysis of MoS_2/$NaTaO_3$/CF (Fig. S3(j)) includes peaks for molybdenum (Mo) and sulfur (S) in addition to sodium, tantalum, and carbon, indicating the successful incorporation of MoS_2 onto the $NaTaO_3$/CF structure.

Supplementary data

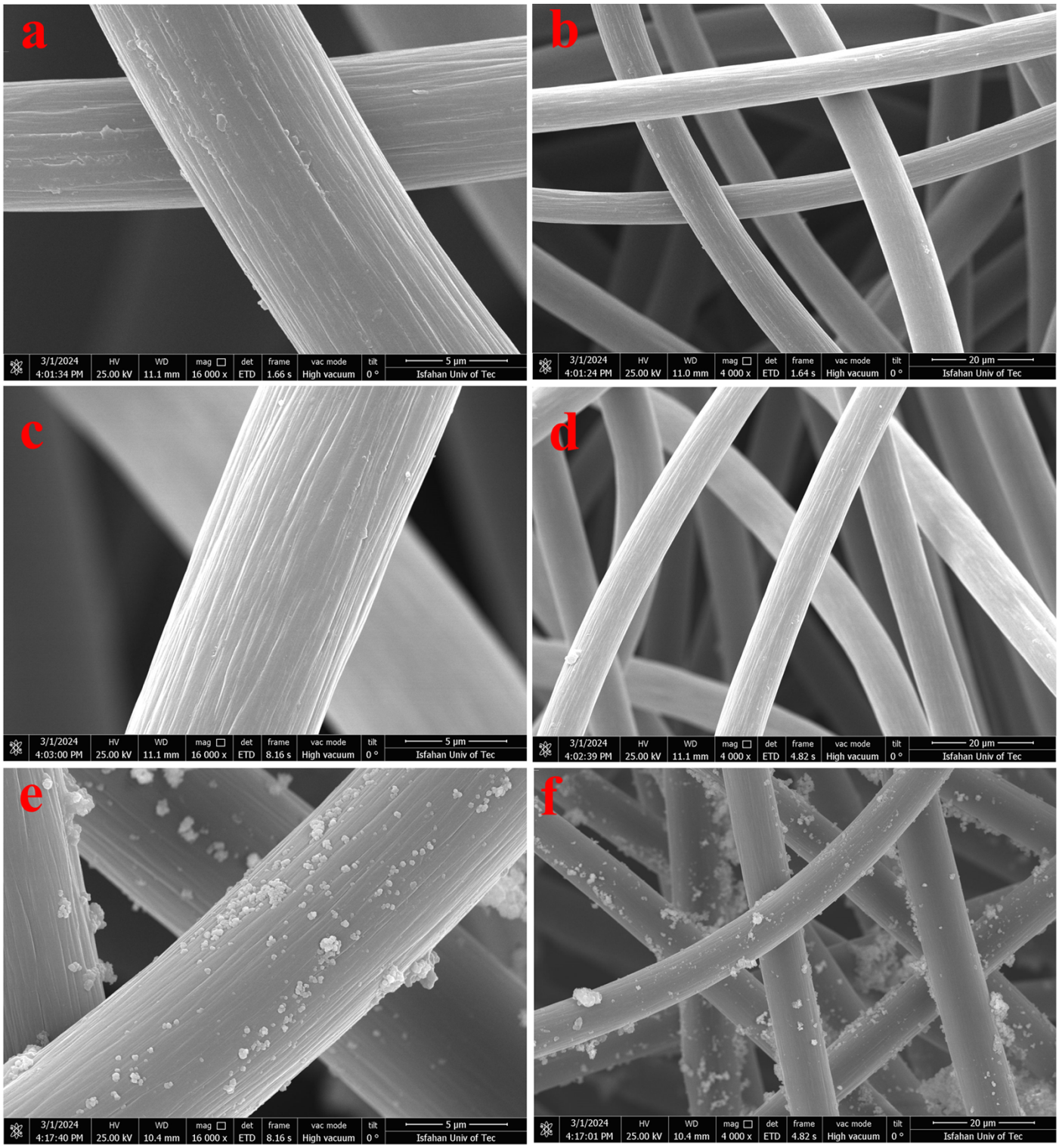

Supplementary data

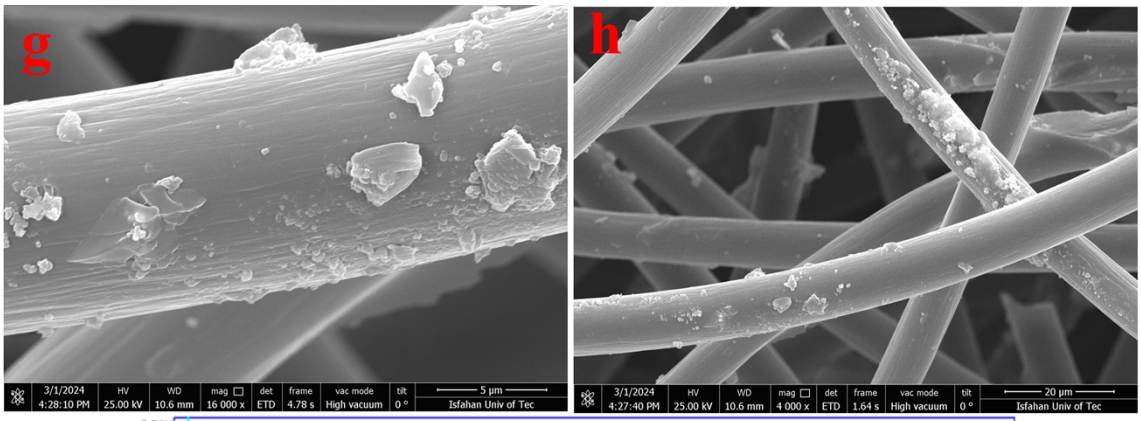

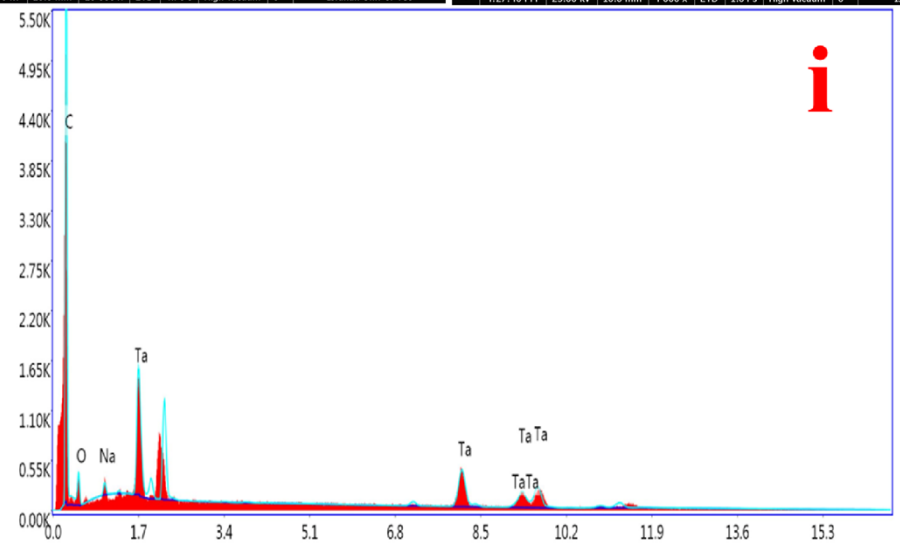

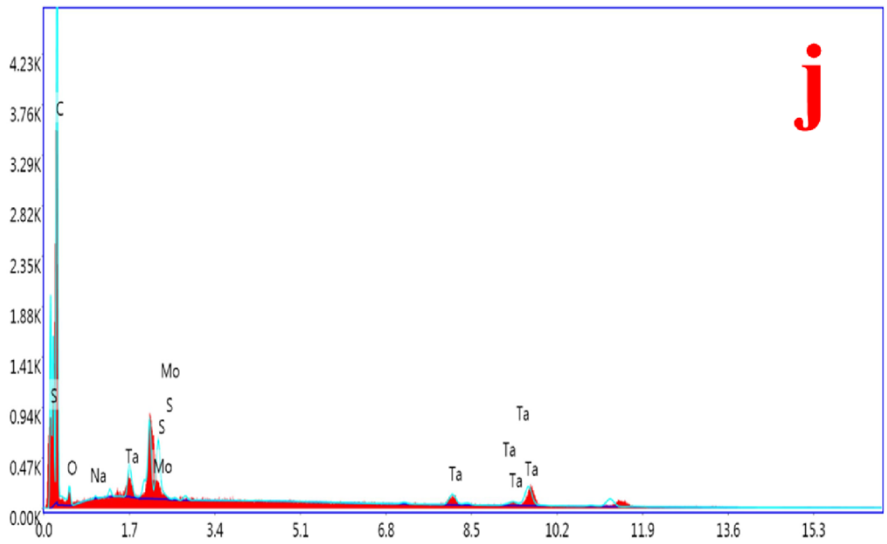

Supplementary data

Fig. S3 FESEM images of (a, b) Carbon felt (CF); (c, d) Activited carbon felt (ACF); (e, f) $NaTaO_3$; (g, h) $MoS_2/NaTaO_3$ and (i, j) EDS spectra of $NaTaO_3$ and $MoS_2/NaTaO_3$.

Comprehensive elemental mapping reveals uniform heterostructure composition. The elemental distribution within the synthesized heterostructures was analyzed through energy-dispersive X-ray spectroscopy (EDS) mapping, as depicted in Figs. S4 and S5. This analysis provides valuable insights into the spatial arrangement of the key chemical components across the carbon felt substrate. The EDS mapping of the $NaTaO_3$/CF heterostructure reveals a homogeneous distribution of sodium (Na), oxygen (O) and tantalum (Ta) signals, indicating the uniform incorporation of the sodium tantalate ($NaTaO_3$) phase onto the flat carbon felt (CF) substrate. This uniform deposition is a desirable structural feature that can contribute to the overall performance and functional properties of the material. Furthermore, the EDS mapping of the $MoS_2/NaTaO_3$/CF heterostructure demonstrates the successful integration of molybdenum (Mo) and sulfur (S) signals in addition to the sodium and tantalum signals observed in the $NaTaO_3$/CF sample. The coherent distribution of all these elemental signals across the carbon-based platform suggests the formation of a multi-layered heterostructure, where the molybdenum disulfide (MoS_2) phase is effectively incorporated onto the pre-existing $NaTaO_3$/CF sample. The comprehensive elemental mapping presented in Figs. S4 and S5 provides direct visual evidence for the successful synthesis of the targeted $NaTaO_3$/CF and $MoS_2/NaTaO_3$/CF heterostructures. This detailed characterization offers crucial insights into the compositional uniformity and structural integrity of the fabricated materials, which are essential for understanding and optimizing their performance in various applications.

Supplementary data

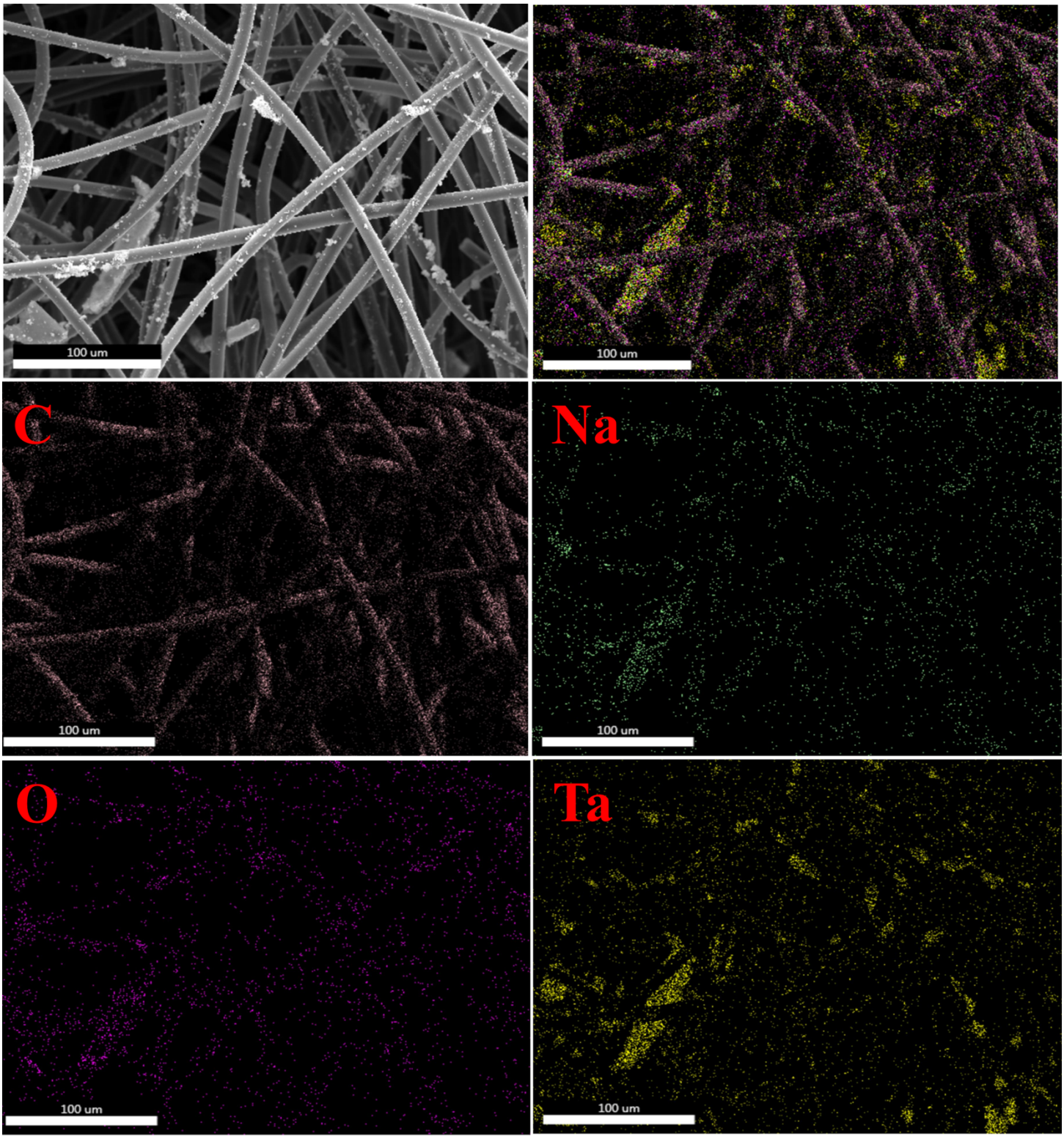

Supplementary data

Fig. S4 EDS element mapping image $NaTaO_3$.

Supplementary data

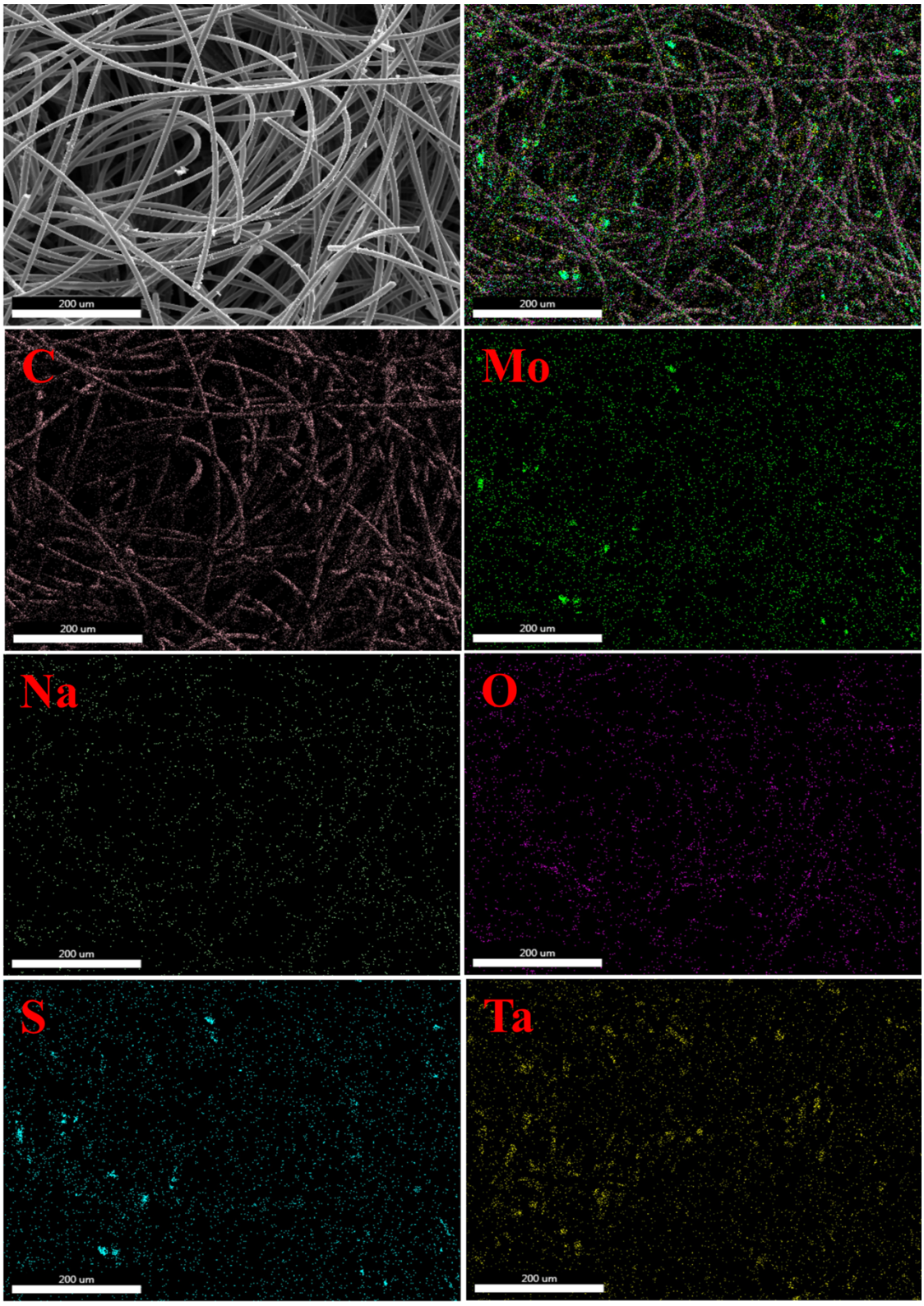

Supplementary data

Fig. S5 EDS element mapping image $MoS_2/NaTaO_3$.

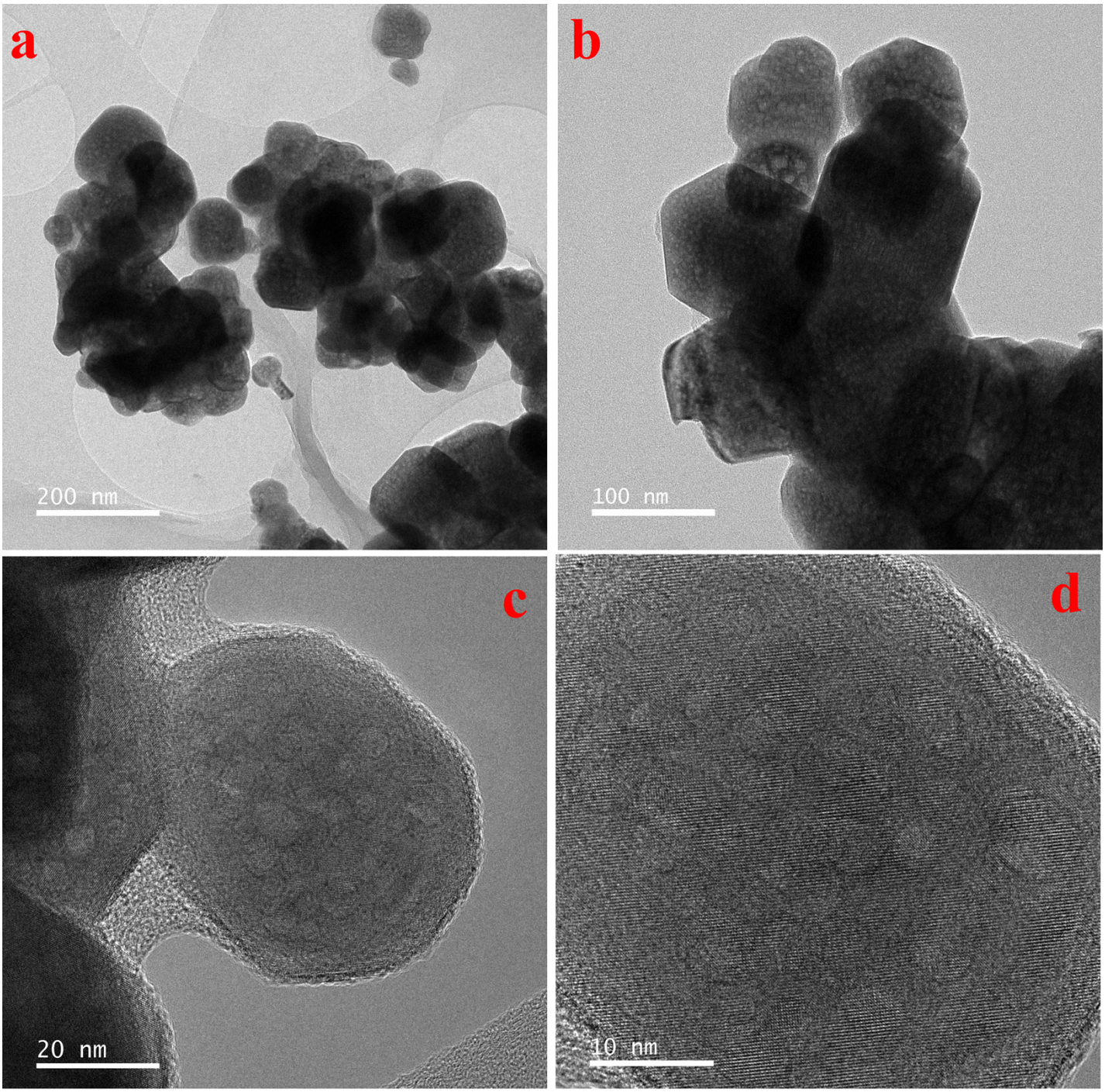

Fig. S6 TEM images, magnified image and HRTEM image of $MoS_2/NaTaO_3$ sample.

Supplementary data

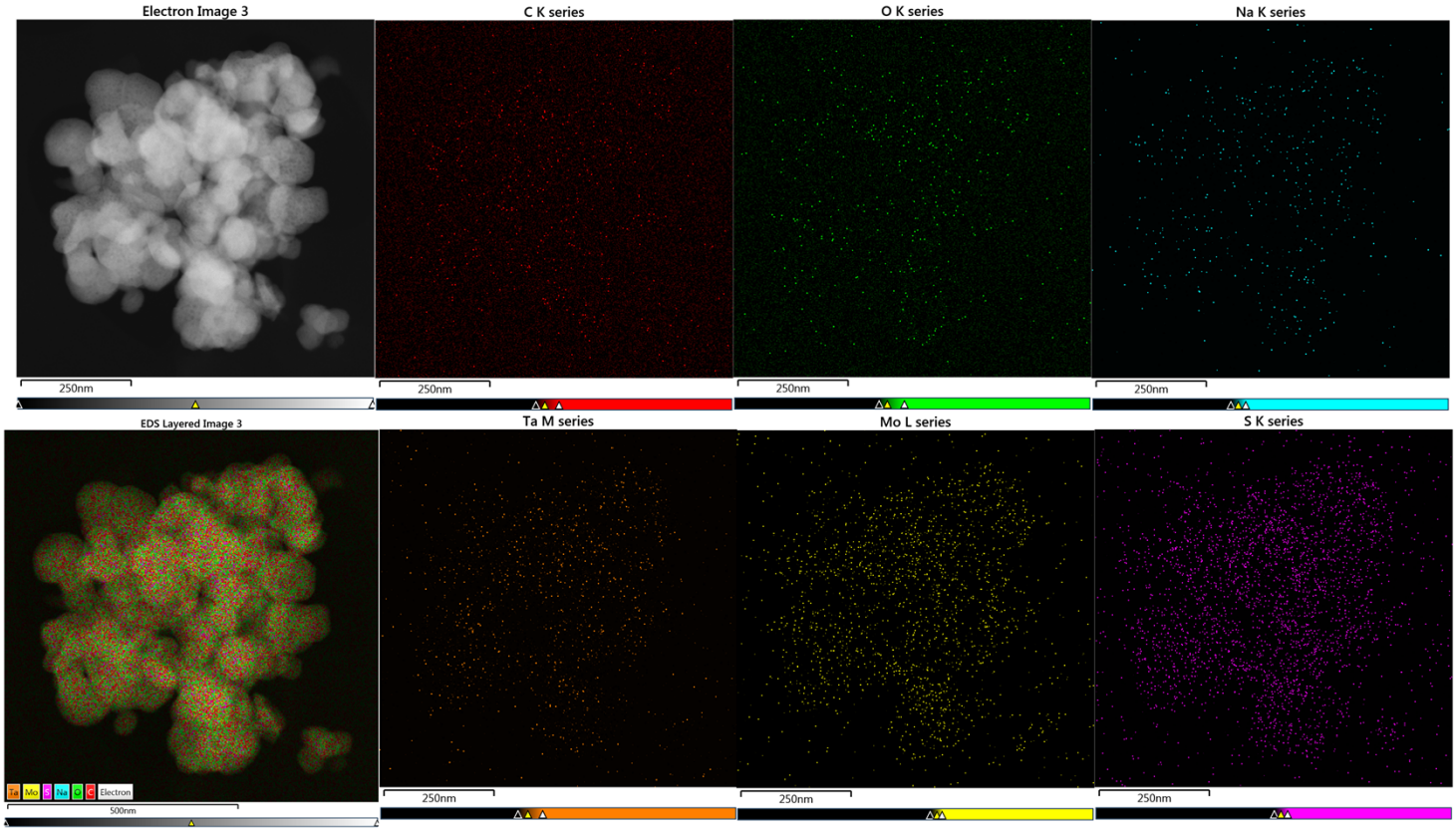

Fig. S7 TEM element mapping images of $MoS_2/NaTaO_3$.

To more precisely uncover the electrochemical behavior of PR-ZIC, Dunn's method was employed to elucidate the energy storage mechanism and electrochemical kinetics of hybrid devices across varying scan rates. The following formulas were used to quantify the variations in the cathode capacitance contribution:

$$i = i_{\text{capacitive}} + i_{\text{diffusion}} = k_1 \upsilon + k_2 \upsilon^{1/2} \quad (1)$$

Supplementary data

$$i/\upsilon^{1/2} = k_1\upsilon^{1/2} + k_2 \quad (2)$$

For both dark and light conditions, the capacitive contribution (black bars) increases with rising scan rates, while the diffusion contribution (green bars) decreases as the scan rate increases (Figs. S7 and S8). Under dark conditions, at a scan rate of 10 mV/s, the capacitive contribution is 26%, whereas the diffusion contribution is 74%. As the scan rate escalates to 500 mV/s, the capacitive contribution increases to 72%, and the diffusion contribution diminishes to 28%. In the presence of light, at a scan rate of 10 mV/s, the capacitive contribution is 17%, and the diffusion contribution is 83%. When the scan rate reaches 500 mV/s, the capacitive contribution rises to 59%, while the diffusion contribution falls to 41%. At lower scan rates, the extended time available allows ions to diffuse deeply into the bulk of the electrode material, thereby causing diffusion-controlled processes to dominate, resulting in a higher diffusion contribution. Conversely, at higher scan rates, the limited time for ion penetration results in surface or near-surface reactions dominating, which are capacitive in nature. Consequently, the capacitive contribution increases. Under dark conditions, the capacitive contribution at low scan rates (26% at 10 mV/s) is higher compared to light conditions (17% at 10 mV/s). However, at high scan rates, the capacitive contribution under dark conditions (72% at 500 mV/s) surpasses that in the presence of light (59% at 500 mV/s). This analysis elucidates the differential electrochemical behavior under dark and light conditions across various scan rates, emphasizing the balance between capacitive and diffusion-controlled processes in energy storage applications.

Supplementary data

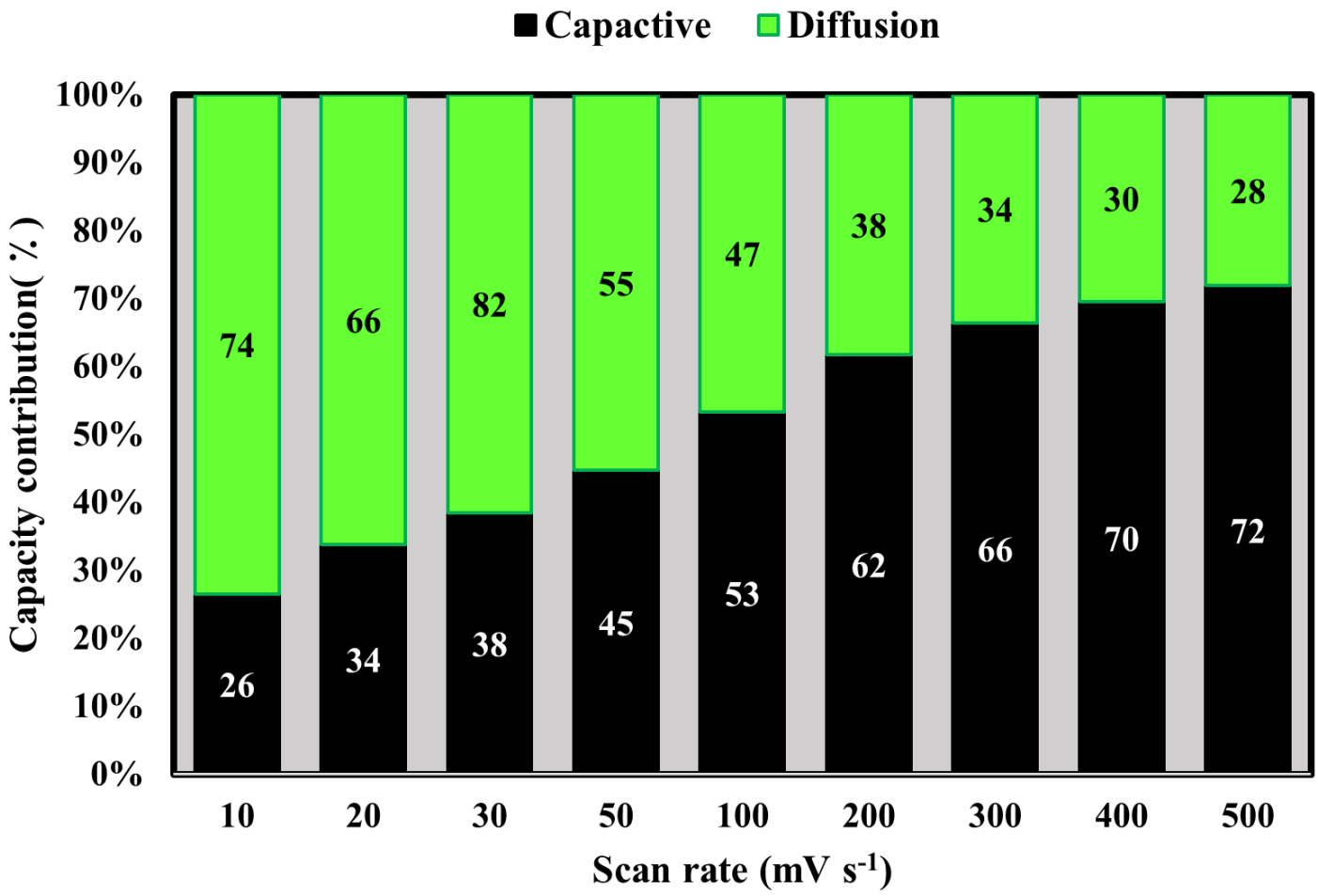

Fig. S8 Capacitance contribution as a function of scan rate in dark condition.

Supplementary data

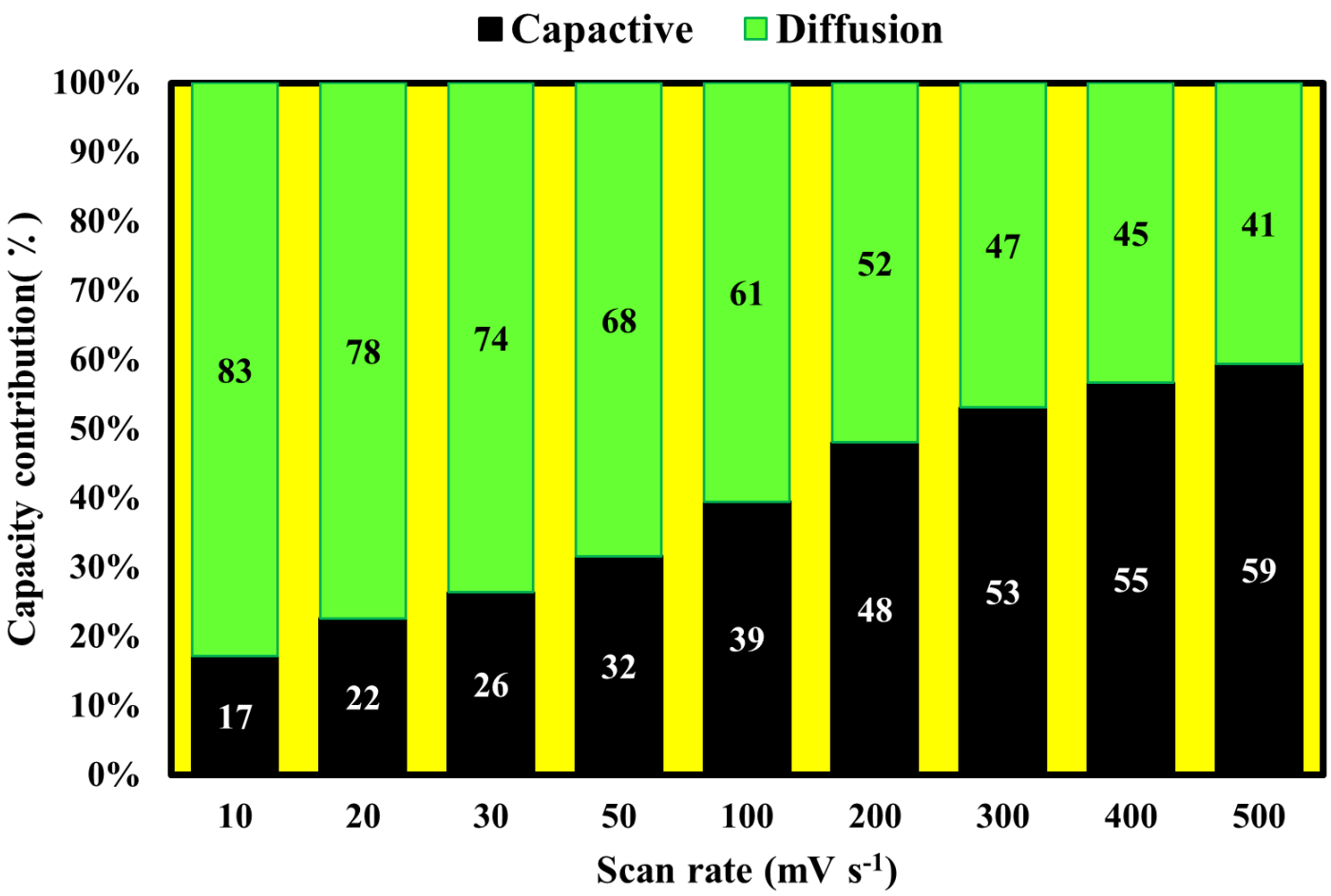

Fig. S9 Capacitance contribution as a function of scan rate under light condition.

Supplementary data

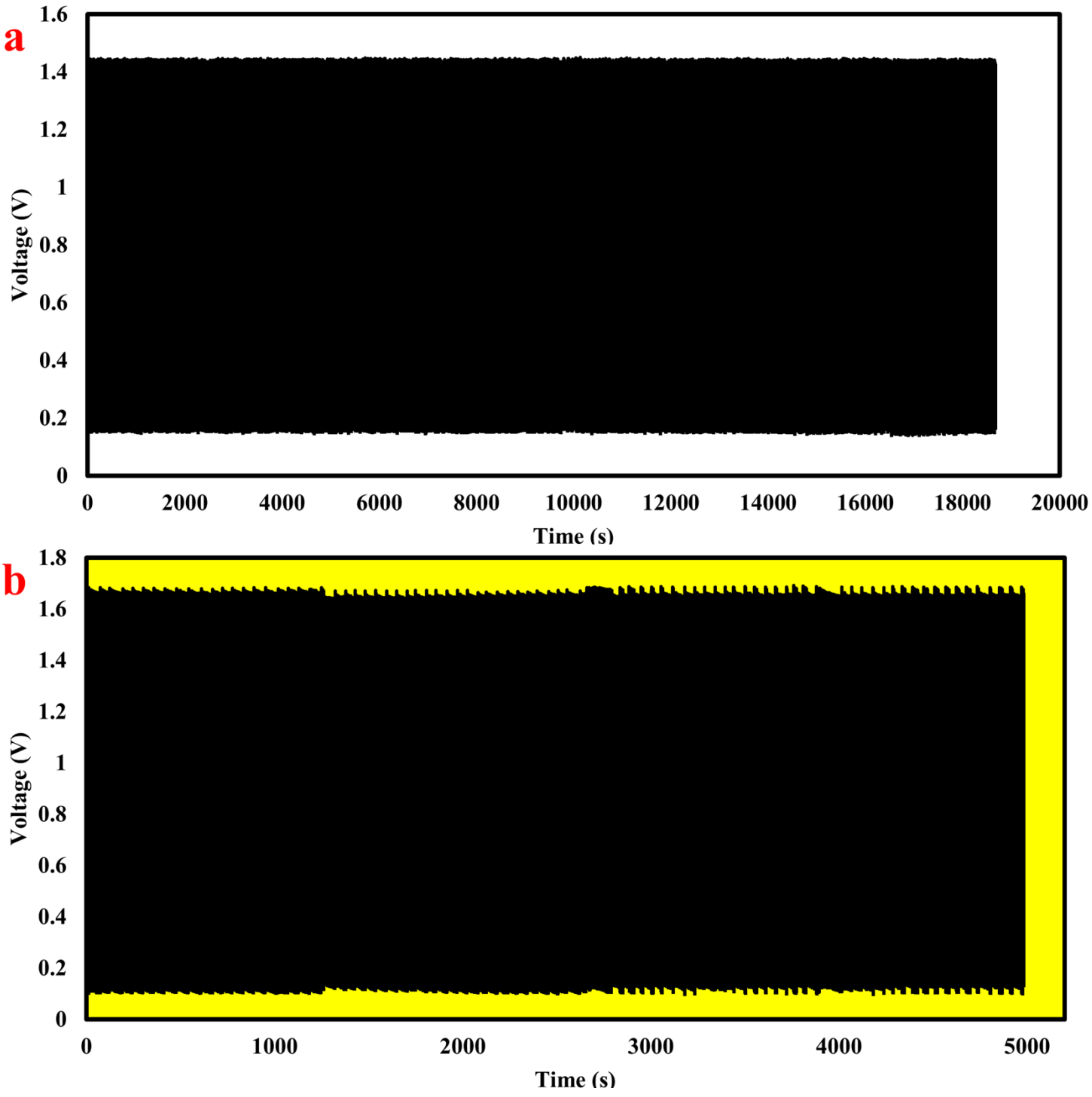

Supplementary data

Fig. 10 (a) Charge-discharge cycling test of PR-ZIC device for 4000 charge/discharge cycles under dark condition and (b) Charge-discharge cycling test of PR-ZIC device for 4000 charge/discharge cycles under light illuminated condition.

The photo-charge conversion efficiency

According to the discharge curve at a current density of 0.1 mA/cm^2 shown in Figure 10a, a specific capacitance of 26.85 mF/cm^2 was achieved. The corresponding energy density (E_s) of the PR-ZIC during the discharge phase was calculated to be 2.63×10^{-6} Wh/cm^2, using the formula [1]:

$$E_s = 0.5\ C_s\times V^2/3600 = Cs\times V^2\ /7200 \qquad (3)$$

Here, C_s (26.85 mF/cm^2) represents the specific capacitance, while V (0.86 V) indicates the operating voltage. Furthermore, the peak photoelectric conversion and storage efficiency (η_t) of the integrated system was approximately 0.23%, determined through the following calculation:

$$E_{output}/E_{input} = E_s.S_1/(P_{input}.t.S_2) \qquad (4)$$

In this equation, E_{output} denotes the energy output of the PR-ZIC, while E_{input} represents the total incident light energy. The variable S_1 corresponds to the surface area of the PR-ZIC, P_{input} indicates the light intensity received, t refers to the duration of the photocharging period, and S_2 represents the effective area of the PR-ZIC.[1]

Supplementary data

Table S1. Comparison of photo conversion efficiency for photo-rechargeable zinc ion capacitors/ zinc ion battery

Sample	Voltage of photo charge	Time of photocharching	Light source	intensity	$\eta_{t(\%)}$	Ref.
Ag@V_2O_5 ZIC	500 mV	1800 s	λ ~ 455 nm	12 mW cm^{-2}	~ 0.05%	[2]
g-C_3N_4 ZIC	850 mV	180 s	λ ~ 420 nm	50 mW cm^{-2}	~ 0.01%	[3]
$Ti_3C_2T_x$ ZIC	930 mV	434 s	λ ~ 420 nm	100 mW cm^{-2}	~ 0.07%	[4]
Te/$Ti_3C_2T_x$ ZIC	930 mV	1585 s	λ ~ 420 nm	100 mW cm^{-2}	~ 0.01%	[4]
VO_2 ZIB	930 mV	15 h	λ ~ 450 nm	12 mW cm^{-2}	~ 0. 18%	[5]
V_2O_5/P3HT/rGO ZIB	950 mV	5 h	λ ~ 450 nm	12 mW cm^{-2}	~ 1.2%	[6]
ZnO/MoS_2 ZIB	950 mV	2 h	λ ~ 455 nm	12 mW cm^{-2}	~ 1.8%	[7]

Supplementary data

MoS_2/SnO_2 ZIB	960 mV	1800 s	xenon lamps	100 mW cm^{-2}	~ 1.0%	[8]
$MoS_2/NaTaO_3$/CF ZIC	860 mV	200 s	xenon lamps	100 mW cm^{-2}	~ 0.23%	Present work

References

1 R. Liu, J. Wang, T. Sun, M. Wang, C. Wu, H. Zou, T. Song, X. Zhang, ST. Lee, ZL. Wang and B. Sun, *Nano Lett*. 2017, **17**, 4240-4247.

2 BD. Boruah, B. Wen, S. Nagane, X. Zhang, SD. Stranks, A. Boies and M. De Volder, *ACS Energy Lett.* 2020, **5**, 3132-3139.

3 BD. Boruah, A. Mathieson, B. Wen, C. Jo, F. Deschler, M. De Volder, *Nano Lett*. 2020, **20**, 5967-5974.

4 J. Azadmanjiri, J. Regner, L. Děkanovský, B. Wu, J. Luxa and Z. Sofer, *Small*. 2024, **20**, 2305972.

5 BD. Boruah, A. Mathieson, SK. Park, X. Zhang, B. Wen, L. Tan, A. Boies and M. De Volder, *Adv. Energy Mater*. 2021, **11**, 2100115.

6 BD. Boruah, B. Wen, S. Nagane, X. Zhang, SD. Stranks, A. Boies and M. De Volder, *ACS Energy Lett.* 2020, **5**, 3132-3139.

7 BD. Boruah, B. Wen and M. De Volder, *ACS Nano*. 2020, **15**, 16616-16624.

Supplementary data

8 XY. Du, LN. Song, S. Liang, YF. Wang, Y. Wang, HF. Wang and JJ. Xu, *Angew. Chem*. 2024, **136**, e202411845.